2024-05-01

Local Map of the Interstellar FUV Field

David Lomeli
University of Texas at El Paso

LOCAL MAP OF THE INTERSTELLAR FUV FIELD

DAVID ALEJANDRO LOMELI

Master's Program in Physics

APPROVED:

_____
Kedron Silsbee, Ph.D., Chair

_____
Jorge Muñoz, Ph.D.

_____
Monika Akbar, Ph.D.

_____
Stephen Crites, Ph.D.
Dean of the Graduate School

to my

MOTHER and FATHER

with love

LOCAL MAP OF THE INTERSTELLAR FUV FIELD

by

DAVID ALEJANDRO LOMELI

THESIS

Presented to the Faculty of the Graduate School of

The University of Texas at El Paso

in Partial Fulfillment

of the Requirements

for the Degree of

MASTER OF SCIENCE

Department of Physics

THE UNIVERSITY OF TEXAS AT EL PASO

May 2024

Table of Contents

List of Figures

Chapter 1

Introduction

The far ultraviolet (FUV) radiation plays an important role in the chemistry of the inter-stellar medium (ISM). The chemical composition of gas in molecular clouds, which play a huge role in the star formation rate in galaxies, is greatly affected by the photoelectric heating caused by photons ranging from 90-206 nm (6-13.6 eV) dominated by the radiation from O and B-type stars. This energy range causes the photodissociation and ionization of many of the molecules and atoms lying in molecular clouds (i.e. H, CO, C). For instance, the FUV radiation photodissociates CO molecules to produce C and O. This C is later ionized by the FUV radiation to make C^+, which acts as one of the most important cooling factors of atomic gas [16][17][10]. The FUV also sets the range of pressures at which cold neutral media and warm neutral media, defined by temperatures on the ranges of 10^2K and 10^4K, respectively, can coexist in local thermal equilibrium as the heating and cooling rates of the medium are faster than the spread of sound waves and turbulent compressions[13]. Therefore, it is of interest to create a map of the local interstellar FUV field to ease the future study of these molecular clouds, or the general study of FUV radiation in the local ISM.

We simulate the direct radiation in the ISM using stellar models and a dust map that allows us to properly account for the attenuation of light due to dust. We use the catalogues PASTEL [15] and Starhorse[1] to account for 857,209 stars with distances up to 1.25 kpc, and with temperatures greater than 7,000K. We also account for extinction using a dust map by [8]. This dust map extends to 1.25 kpc away from us, and hence establishes a max-imum distance on the set of stars being used. These catalogues supply enough information such that the FUV flux, stellar radius, and distance can be calculated for this set of stars.

We use this information to calculate the energy density contributed by direct radiation in the FUV to create a map with the shape of a sphere with a radius of 800 pc.

1.1 Dust

Dust in the ISM is composed of hydrocarbons and silicates[14] which absorb and scatter light, therefore attenuating it. Just as in a dust storm, it is hard to see through it. That is, since light coming from the other side of the dust storm is being absorbed by the dust in the dust storm, it is not reaching your eyes unattenuated. This same principle applies to the ISM. The higher the column density of dust which light passes through is, the less light will pass through unaffected. We will ignore the effects of scattered light. Whether this effect is ultimately negligible within the volume in the ISM in consideration requires further careful study. Previous measurements of the diffuse radiation here at Earth range between 8-11% of the total FUV field[9] for different wavelengths. However, this ratio can't be assumed to be constant throughout the volume of the ISM in consideration.

1.2 Energy Range

We take into consideration the wavelength range from 90-206 nm which corresponds to 6-13.6 eV. The upper bound on this energy range is defined by the ionization energy of hydrogen in its ground state. Photons with energy beyond this range are quickly absorbed and scattered due to a sphere of hydrogen surrounding stars. This sphere is known as the Strömgren sphere. If a hot star is surrounded by a cloud of uniform dense gas, there will be a region of completely ionized hydrogen where the recombination and ionization rates are equal [14]. The size of the Strömgren sphere is defined by the Strömgren radius. For clarification, if the region surrounding the star is not uniformly dense, this will result in the Strömgren sphere not being spherical. However, it is still true that ionizing radiation does not travel far. For explanation purposes, these regions will be assumed to be spherical.

Therefore, since the energy required to ionize hydrogen is 13.6 eV, any photons emitted by the star with E $\geq$ 13.6 eV will be used to keep the ionization and recombination rate the same within this sphere, and the emitted and scattered photons, other than Lyman alpha, beta, and gamma photons, from recombination will be of lower energy and therefore ignored for our purposes. These high energy photons (E $\lessapprox$ 13.6 eV) will make it past this sphere due to diffusion velocities of gas in the sphere.

1.3 Transmission Filters and Magnitudes

Astronomers have adopted the magnitude convention for labeling the brightness of stars. A star's apparent magnitude is a description of how bright a star appears in the sky, or better put, how much light we receive from this star. By convention, if we compare two stars where one emits 100 times the flux of the other, the star emitting the higher flux will be 5 magnitudes lower, or 5 magnitudes brighter, than the dimmer star. Therefore, higher magnitudes correspond to dimmer stars. To compare the magnitudes between stars, the following equation is used:

$$m_2 - m_1 = 2.5 \log \frac{F_1}{F}, \quad (1.1)$$

where m_1 and m_2 are the apparent magnitudes of two stars, and F_1 and F_2 are the respective bolometric fluxes, or the flux received across the electromagnetic spectrum. For convention, log() will be used to denote a base-10 logarithm and ln() will be used for base *e*. It is one convention to compare magnitudes, or label the zero-point to the star Vega as it is among the brighter stars in the sky and it varies little in luminosity. The flux received can be filtered within some wavelength range using transmission filters and these have been widely used across multiple satellite and observatory missions.

One of the most popular transmission filter systems is the Johnson-Cousins system, also known as the UBVRI system, as per its separately named filters: U (Ultraviolet), B (Blue), V (Visual), R (Red), and I (Infrared). If the V band magnitude is desired, the first step is

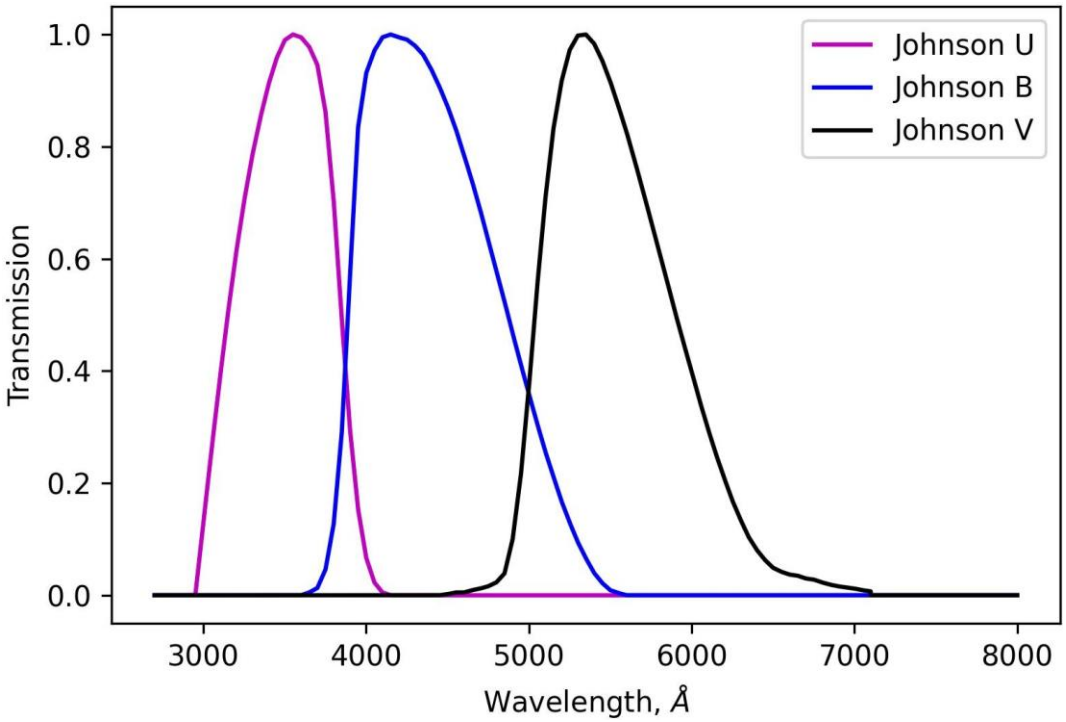

Figure 1.1: Johnson U, B, and V transmission filters.

to change the flux measurement as follows:

$$F_V = \frac{1}{hc} \int_0^\infty F_\lambda T_V(\lambda)\, \lambda d\lambda, \tag{1.2}$$

where F_λ is the flux per wavelength, $T_V(\lambda)$ is the transmission value per wavelength of the V band, F_V is the number photons per area per unit time that pass through the filter, and h and c denote Planck's constant and speed of light, respectively. If F_V is wanted in units of energy per area per unit time, then the factor of λ/hc is removed from the integral. $T(\lambda)$, is the fraction of photons with wavelength λ that pass through the filter. These values change for different wavelengths and filters. Additionally, different transmission filters have different zero points. This point can be treated as a calibration value among filters to create consistency between these. As mentioned before, it is convention to treat the zero point in such a way that the star Vega has a magnitude of 0. Vega varies slightly in magnitude, and therefore the appropriate way to calibrate a filter is by comparing its spectrum and its spectral energy distribution (SED). By doing so, monochromatic fluxes can be calculated for different spectral types of stars. For instance, the star Vega, whose spectral type is A0, has a monochromatic flux of 3.631×10^{-9} erg/s/cm^2/Å at $\lambda = 5450$Å[3]. This results in a magnitude of 21.1, which is the zero-point of the ST-MAG system. Further discussion is provided in §2.5.

Similar to the V band, there is the Tycho V band seen in Figure 1.2. We use the stellar magnitudes with this filter to estimate the radii of stars in the PASTEL catalog.

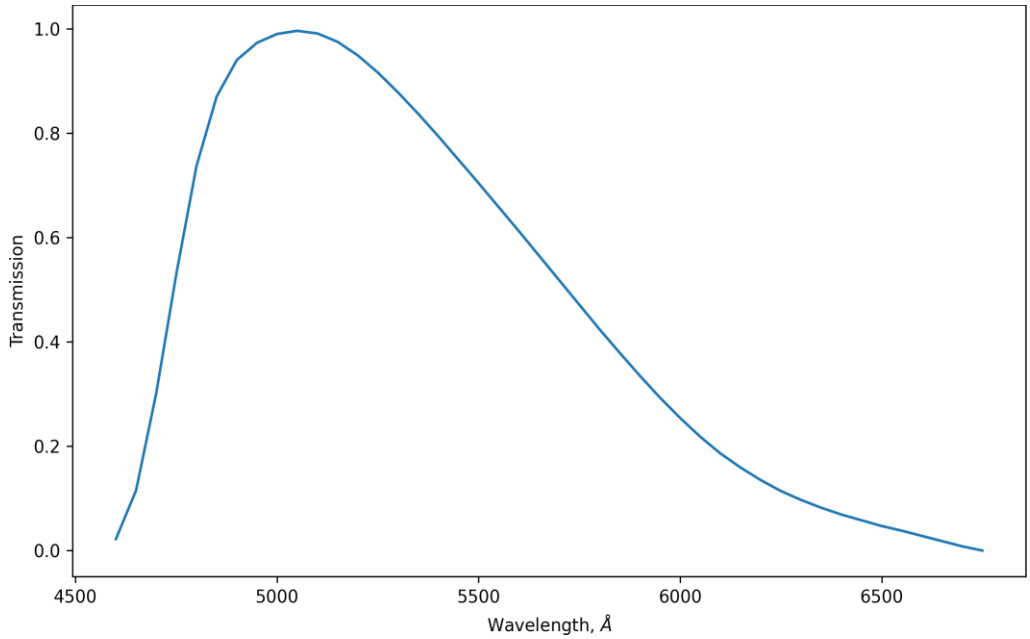

Figure 1.2: Transmission plot of the Tycho (V_T) band.

Chapter 2

Methodology

2.1 Coordinate Systems

Catalogues label a star's coordinates using different coordinate systems. For instance, Starhorse uses stars from the third early data release of GAIA, or GAIA EDR3. GAIA returns the coordinates of these stars in galactic spherical coordinates (l, b). This coordinate system uses the Sun as the origin, and comprises of its angular elements l and b, the galactic longitude and latitude. These behave the same as the longitude and latitude on Earth, but l=0 points to the center of the galaxy, and b=0 is the galactic plane. Starhorse however, reports the coordinates of stars in a cartesian galactocentric format. The origin of this system is at the center of the Galaxy, assumed to be 8.2 kpc away from us. This system's $\hat{x}$ coordinate points to the direction opposite to Earth, the $\hat{y}$ direction is the opposite direction of motion of the solar system around the galaxy. Lastly, the $\hat{z}$ direction points along the vertical axis, following the convention of a right-handed coordinate system. Therefore, to transform these coordinates to cartesian galactic coordinates, the 8.2 kpc is added to the $\hat{x}$ coordinate. The remaining coordinates stay the same. The distance between the Sun and the galactic plane of approximately 20 pc is also accounted for from the data from Starhorse.

A different set of coordinates used by catalogues is the equatorial coordinate system. This system follows the same format as the galactic coordinate system, but instead of l and b, the equatorial coordinate system uses right ascension (α) and declination (δ) along the Earth's equator where $\alpha = 0$ points at the vernal equinox. The vernal and autumnal equinoxes are the nodes corresponding to the points of intersection between the equatorial

and ecliptic planes. The ecliptic plane is the plane denoted by the Earth's motion around the Sun, while the equatorial plane is the plane denoted by the Earth's equator. These two planes vary by 23.5°. This tilt, or difference between these planes is also called the 'obliquity of the ecliptic.' Considering the equatorial coordinate system, the vernal equinox is found at the point where the Sun moves from the southern to northern hemisphere. The opposite is true for the autumnal equinox.

2.2 Parallax

Parallax is the apparent angular displacement of an object when viewed from a different point of view. As per Figure 2.1, the parallax angle ϑ will be smaller at longer distances, d. If we consider the Earth moving around the Sun to observe a star at a distance d and parallax angle ϑ:

$$\tan(\vartheta) = \frac{1\text{AU}}{d}$$

By doing a small angle approximation and transforming degrees into arcseconds (”),

$$d = \frac{1\text{AU}}{\vartheta''} \quad \frac{180^\circ}{\pi} \quad \frac{3600''}{1^\circ} = \frac{206,265\text{AU}}{\vartheta''}. \tag{2.1}$$

206,265 AU becomes the official definition of a parsec, or the 'parallax of one arcsecond.' Therefore, this can be written as:

$$d = \frac{1}{\vartheta''}[pc]. \tag{2.2}$$

where the resultant distance is in parsecs.

2.3 Stellar Models

In order to calculate the UV output for each star, we made use of the stellar atmospheric models by [6]. These models give a list of values for discrete wavelengths of the specific intensity, H_ν, or the net flux density per frequency averaged over all solid angles, based on

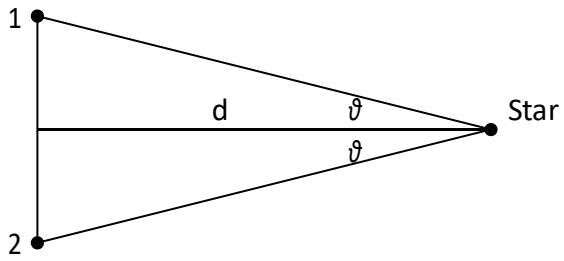

Figure 2.1: Schematic diagram of the parallax effect where Points 1 and 2 are observation points. Note that at Point 1, the star is 'below' the observer, and at Point 2, the star is 'above' the observer. This change in perspective allows satellites to calculate the distance to far-away objects.

a star's log(g) and effective temperature, T_{eff}. A star's log(g) is the base-10 logarithm of the star's surface gravity in cgs units. A star's T_{eff} is the temperature assigned to a star that emits the same bolometric flux according to Stefan-Boltzmann's Law $F_{bol} = \sigma_{SB} T^4$. We found there to be a negligible difference between the energy density from these stellar models with varying log(g) however, as seen in Figure 2.2. We therefore assumed our sample of stars to have log(g) = 4, unless the models required a higher log(g) due to higher temperature stars only having stellar models with log(g) $\geq$ 4.0. For these cases, a log(g) of 5.0 was used. We can then calculate a star's flux in the FUV at its surface in the following manner. If H_ν is the net flux density per frequency averaged over all solid angles, we can further integrate this value over all solid angles over some frequency range [ν_1, ν_2] as follows:

$$F_{FUV} = \int_0^{\pi} \sin(\vartheta) d\vartheta \int_0^{2\pi} d\phi \int_{\nu_1}^{\nu_2} H_\nu d\nu \tag{2.3}$$

We can also include the following change of variables:

$$\nu = c/\lambda$$
$$d\nu = \frac{c}{\lambda^2} d\lambda$$

Therefore, if we integrate over the wavelength range [90nm, 206nm]:

$$F_{FUV_S} = 4\pi c \int_{90nm}^{206nm} \frac{H_\nu}{\lambda^2} d\lambda \tag{2.4}$$

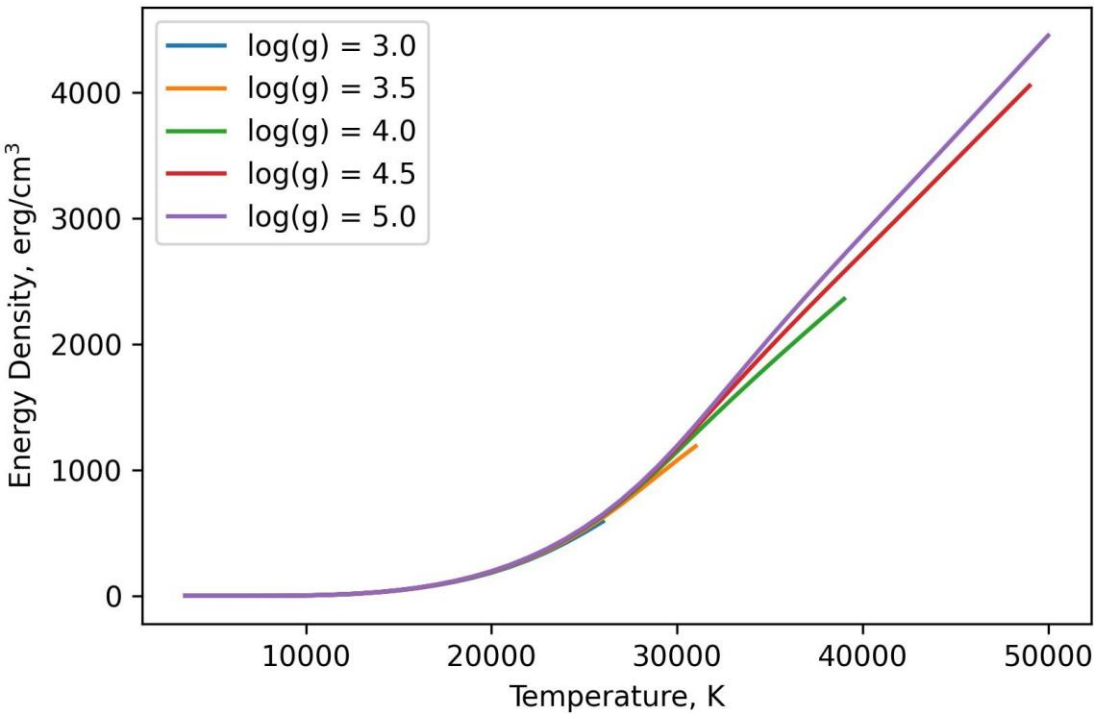

Figure 2.2: Energy density as a function of T_{eff} for varying log(g) among different stellar models from Castelli and Kurucz [5]

This yields the total radiation flux in the FUV that a star emits for a specific temperature and log (g). However, the stars' T_{eff} is not always going to be exactly the temperature described by these models. Therefore, we perform a linear interpolation between the two closest models.

2.4 Extinction

Dust along the line-of-sight from a star to a specific point will attenuate the flux that said point will receive in an exponential manner related to the dust's optical depth, τ . More specifically,

$$F_{FUV_C} = F_{FUV_P} e^{-\tau}, \tag{2.5}$$

where F_{FUV_C} is the flux at the point of interest after extinction and F_{FUV_P} is the flux at the same point excluding extinction. τ can be thought about as the number of e-folds that light is reduced by when passing through a column of dust. It has a more formal definition as follows:

$$\tau = \int_0^l \sigma n(z) dz \tag{2.6}$$

where σ is the attenuation cross section of the material, and $n(z)$ is the number density of said particles along the column line of sight of length l.

2.5 Dust map

We use a dust map from [8] to account for the extinction due to dust in the local ISM. This map, seen as a projection in Figure 2.3 gives a detailed overview of the 3D dust density in the ISM. The dust map is made by doing an inference analysis on GAIA stars and extinctions coming from [18]. GAIA is the name of the satellite that records positions, radial velocities, proper motions, and magnitudes from billions of stars using its own G-band transmission filter. Simply put, if we take two stars whose angular separation is small, but distance is different, we can infer how much dust there is between these two

stars by looking at their extinction values. The star that is further away, will have a higher extinction, and this difference is used to infer the dust density between these two stars. The dust map used is a sphere of radius 1.25 kpc with a spherical hole of radius 69 pc with the Earth in the center. The dust map can be interpolated onto a grid of a desired grid size so as to make a 3D grid that can be accessed through indexing. We chose a grid spacing of 5x5x5 pc^3. The values given by the map are in the form $\frac{A_V}{2.8}$/pc, where A_V is the spectral absorption in the V-band. We further multiply these values by $\frac{2.8 \ln 10}{2.5}$ in order to get these values into $\tau_{UV(\lambda)}$, where the $\frac{\ln 10}{2.5}$ factor is the general conversion factor between A_V and τ_V. The relationship between these is derived as follows:

The observed flux after extinction is defined as:

$$F_{obs} = F_0 e^{-\tau}, \tag{2.7}$$

where F_0 is the flux that would be observed in the absence of dust. We then convert to magnitudes using the most general form of the Pogson Equation [3]

$$m = C - 2.5 \log(F),$$

where m is the apparent magnitude of the star, and C is the zero-point of the filter. Knowing this, we get the following:

$$m_{obs} = C - 2.5 \log(F_0) - 2.5 \log(e^{-\tau}).$$

Furthermore,

$$m_{obs} = m_0 + \frac{2.5}{\ln 10}\tau,$$

where m_0 is the apparent magnitude in the absence of dust. Therefore, solving for τ,

$$\tau = \frac{\ln 10}{2.5}\Delta m, \tag{2.8}$$

where Δm is the difference in magnitude caused by extinction, or A.

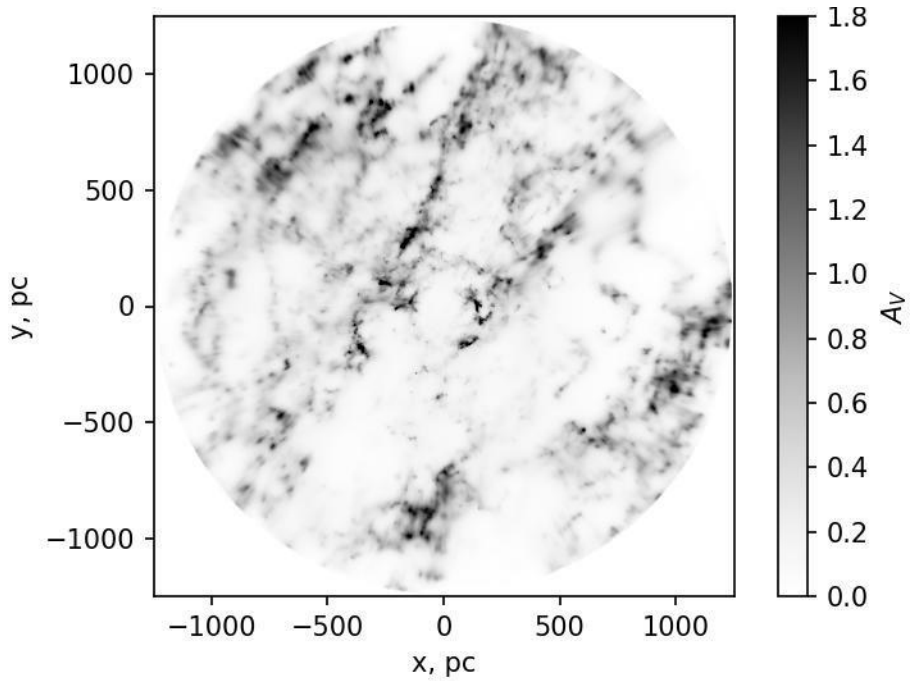

Figure 2.3: Projection of the dust map from [8] with a resolution of 5*5*5 pc^3. The color bar is linear and was adjusted to better show the features of the dust map. Since the map is a sphere of 1.25 kpc, the value of the differential extinction is assumed to be 0 in this plot.

2.6 Extinction Curve

Eq. 2.7 is generally correct when considering a measurement for one specific wavelength, or when τ is constant across all wavelengths. However, another caveat within our calculations is that extinction is wavelength-dependent. Higher temperature stars whose spectrum peaks at shorter wavelengths will tend to experience higher extinction than lower temperature stars whose spectrum peaks at longer wavelengths due to the rate of absorption at different wavelengths. In order to account only for the FUV, we make use of the following extinction curve replicated from [4]referred to as the CCM extinction curve.

It is standard to choose R_V =3.1, as this is the standard value in the solar neighborhood[14],

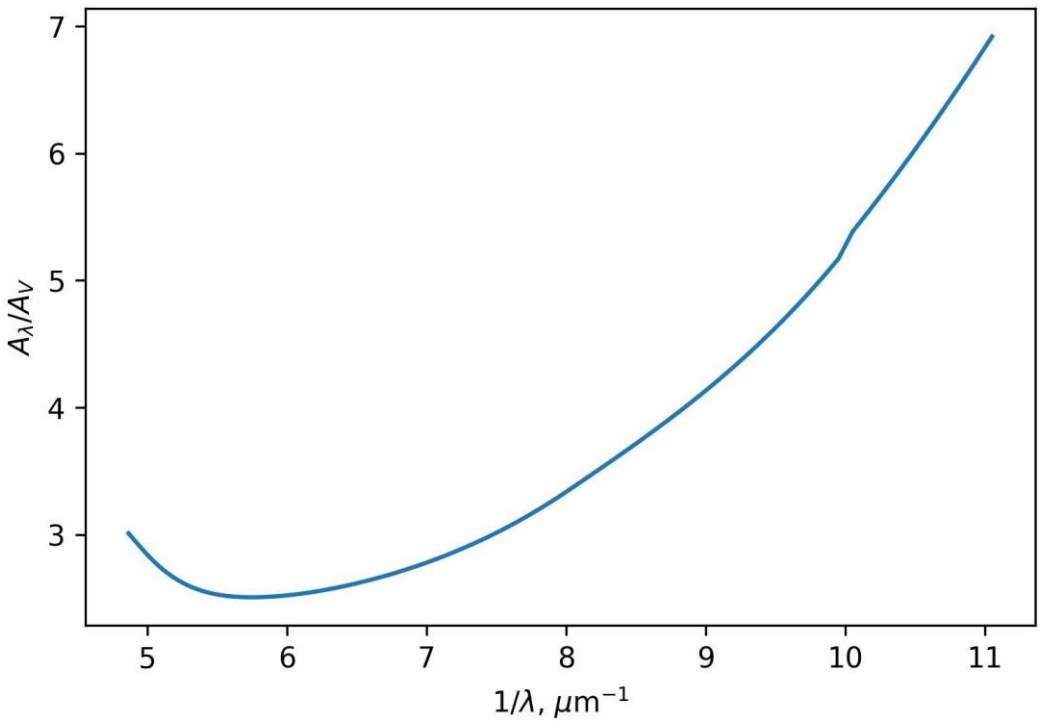

Figure 2.4: Extinction curve for λ = (90nm, 206nm) from [4] with R_V = 3.1. Values beyond 10 μm^{-1} were extrapolated with a second degree polynomial fit.

for the total to selective extinction ratio defined by $R_V = A_V/E(B-V)$, where $E(B-V)$ is the color excess, or the difference between the observed and visual color of an object. By extracting the A_V value along the line of sight from the dust map, we convert it to A_λ by multiplying it by the proper value from the CCM curve based on the wavelength in consideration.

This curve is not defined for the range 90-100 nm however. To account for the missing wavelength range, we used an extrapolation method using a second order polynomial fit to estimate the values in the missing wavelength range.

To further decrease the computation time, we incorporated an approximation based on this extinction curve and the stellar spectra. By dividing this curve into 3 parts (90-130nm, 130-170nm, and 170-206nm), we can get the average value of A_λ/A_V along each division and use that value as the corresponding A_λ/A_V for that wavelength range. The spectra for the stars are divided in the same way. Each division of the spectra is then integrated and written into a file. This allows us to efficiently calculate the flux at a specific point after attenuation as we only need to calculate three different extinction factors.

2.7 Geometric Attenuation

As a star emits light and this spreads out over some distance, the amount of light received by some surface area in space decreases as the area is further away. The surface integral of the flux emitted by a star is the same for spheres of different radii however, assuming no extinction, as seen in Figure 2.5. In other words,

$$\int\int_A F_P \cdot dA_{r=D} = \int\int_A F_S \cdot dA_{r=R}$$

$$4\pi F_P D^2 = 4\pi F_S R^2$$

where F_S and F_P are the flux calculated at the star's radius and at a point at a distance

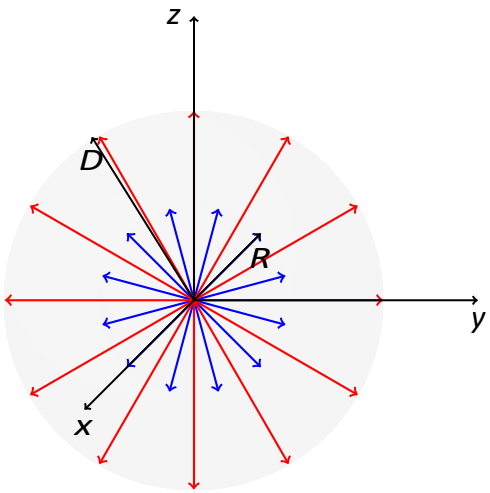

Figure 2.5: The total flux of light at different radii will be the same as long as the star emits light and there are no intensity attenuations. The blue arrows represent the photons leaving the star at a radius R, whereas the red arrows represent the same photons leaving a sphere of radius D.

D from the star, respectively. Therefore, it is easy to see that,

$$F_P = \left(\frac{R}{D}\right)^2 F_S. \tag{2.9}$$

The $\left(\frac{R}{D}\right)^2$ factor is called the geometric attenuation. Including both the geometric and dust attenuation of every star, Equation 2.9 becomes:

$$F_{FUV_C}(\lambda) = \left(\frac{R}{D}\right)^2 F_{FUV_S}(\lambda)\, e^{-\tau_{FUV}(\lambda)}. \tag{2.10}$$

To relate the flux and energy density, we use the electromagnetic properties of photons. Electromagnetic flux is defined as follows:

$$F = S \times \hat{n}$$

where S is the Poynting vector, and $\hat{n}$ is the normal vector relative to the surface at which the energy is flowing. Therefore,

$$F = \frac{1}{\mu_0} E \times B \cdot \hat{n}.$$

Knowing that energy density is defined as:

$$u = \epsilon_0 E^2,$$

and that the ratio between the electric and magnetic fields is c, the speed of light

$$E/B = c = 1/\sqrt{\mu_0 \epsilon_0},$$

it can be derived that,

$$F = cu. \tag{2.11}$$

Ultimately, the contribution from a particular star to u_{FUV} can be calculated from Eq. 2.10 and 2.11,

$$u_{FUV_C}(\lambda) = \left(\frac{R}{D}\right)^2 \frac{F_{FUV_S}(\lambda)}{c} e^{-\tau_{FUV}(\lambda)}. \tag{2.12}$$

Chapter 3

Catalogue Collection

We use the information in [15] and [1] to construct a catalogue of relevant parameters for the stars used in our study. For stars that are in both catalogues, we adopt the parameters from [15]. The only stellar parameters needed are the stars' T_{eff}, a way to measure the star's radius, and its coordinates. We aim to have as close of a result to the true value of the FUV energy density while minimizing computation time. Therefore, we included some constraints when cataloguing our pool of stars.

3.1 Effective Temperature

Figure 3.1 shows that the sum of the individual energy density measurements from all stars in the FUV, or cumulative energy density in the FUV, u_{FUV}, as a function of temperature starts to plateau at T $\leq$ 7000K, as 99.92% of the total energy density coming from stars within the dust map is recovered. Therefore, it is shown that at the Sun, the total contributions to the u_{FUV} of stars with $T_{eff} \leq$ 7000K can be ignored in our sample, hence greatly reducing the number of stars in consideration. Since the stellar models being used are being interpolated between the (T, log(g)) segments, the jumps in the plot are caused by specific stars nearby the Sun.

3.2 Distance

Another constraint we considered is that the dust map being used is of finite size. Therefore, so as to include only stars within the dust map, we used stars with distance $\leq$ 1.25 kpc.

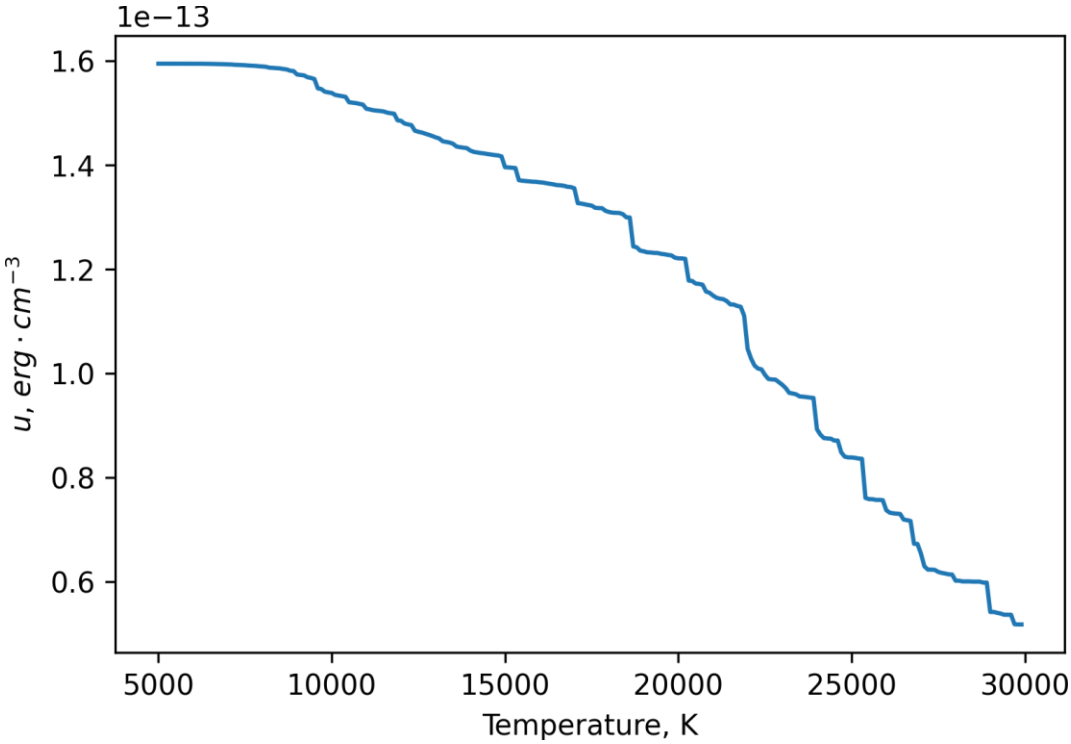

Figure 3.1: Cumulative energy density with temperature cutoff without taking extinction into consideration. At any point (T,u) along this line, only the stars with temperatures greater than T are considered in the contribution to the total energy density. A plateau starts to form around T = 7000K, and hence we can neglect stars with temperatures lower than 7000K as their contribution would be negligible and increasingly computationally expensive.

Figure 3.2 shows the normalized cumulative energy density contributions of stars with distances less than the specific x-coordinate in the graph, considering extinction at Earth. At Earth, ∼90% of the energy density is recovered for stars within ∼600 pc. For PASTEL, we used the Hipparcos parallax to measure distance. For Starhorse, a distance measurement of **dist50** in the catalogue was used. This is the median posterior output value acquired from the analysis done on GAIA EDR3 stars to make up Starhorse. SkyCoord, a python package that allows for the transformation of coordinates between different frames was used

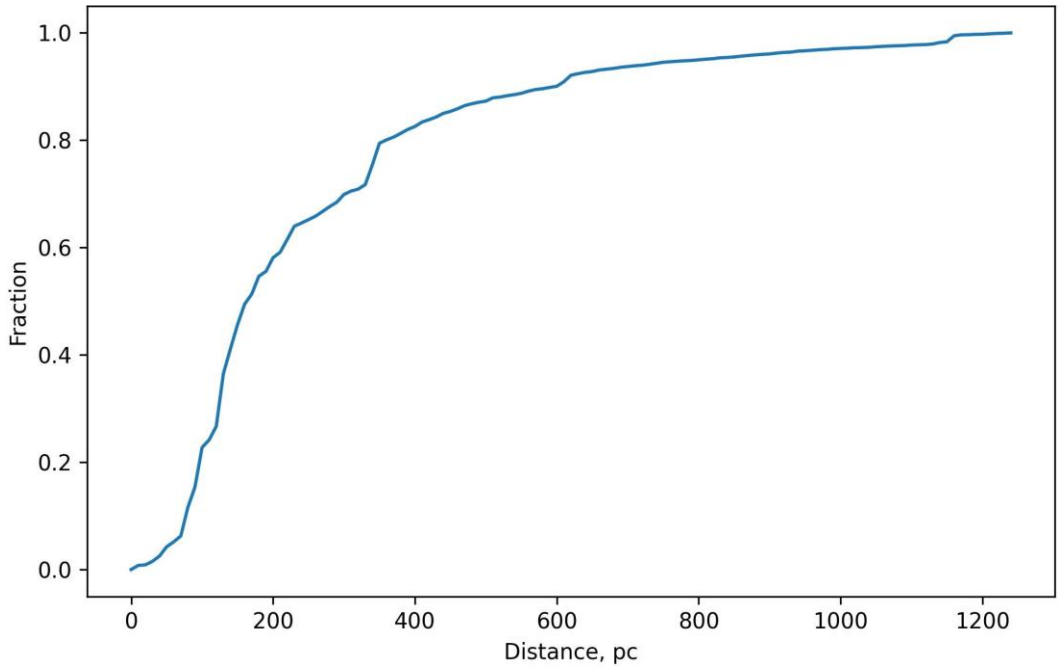

Figure 3.2: Normalized cumulative energy density at the Sun based on a distance cut. For a specific (x, y) value along the plot, only stars with distance less than or equal to x are considered in the calculation of the energy density at the Sun. Sharp changes in the continuity in the plot are caused by individual high temperature stars.

to convert equatorial coordinates to cartesian galactic coordinates.

3.3 Radius

The two catalogues provide values for different sets of stellar parameters and therefore we use different methods to calculate the stellar radii in each case.

- If a star's log(g) and mass are given, as it is the case in Starhorse, we promptly calculate a star's radius in the following manner:

$$g = \frac{GM}{R^2}$$

$$R = GM/10^{\log(g)}{}^{1/2}. \tag{3.1}$$

- Otherwise, for the stars in PASTEL, we get the star's V_T-band apparent magnitude and corresponding stellar models based on the stars' temperatures to solve the following equation from [2]:

$$m_V + 2.5 \log \left(\frac{R}{D} \right)^2 \frac{\int F_\lambda e^{-\tau(\lambda)} T_V(\lambda) \lambda d\lambda}{\int \frac{T}{\lambda}} + 48.6 - 0.037 = 0, \tag{3.2}$$

$$R = D \sqrt{10^{-19.4252 - m_{VT}} \cdot \frac{\int T_{V_T}(\lambda) c \, d\lambda}{\int \frac{T_{V_T}(\lambda) c}{\lambda} d\lambda}} \tag{3.3}$$

where T_{V_T} is the V_T-band transmission curve, and F_λ is the flux calculated with the appropriate stellar model. The distance to said star is calculated from its parallax.

Chapter 4

Precalculations

When considering the entire sample of stars to make the map, we have to be careful when choosing from where we get our data. PASTEL is prone to having repeated instances of the same star, although the data is essentially unaffected, if slightly different. Additionally, PASTEL has stars that Starhorse has as well. PASTEL, on its own has repeated instances of the same star. Establishing a hierarchy between these two catalogues is necessary to choose from where will the information be used for the set of repeated stars between PASTEL and Starhorse.

Additionally, there is a choice to be made regarding the map size and resolution. We want to be careful to not make the map so large that the stars outside of the dust map contribute significantly to the FUV field within the map because the stars from outside the dust map can't have their extinctions calculated with the dust map in use. Furthermore, we want to be careful to choose an appropriate resolution such that the star distance errors from the catalogues are not too important to the overall structure of the map. Optimally, we want to choose a resolution that is more than the average distance error to stars.

4.1 Catalogue Hierarchy

If a star is both in PASTEL and Starhorse, the parameters from PASTEL will be used. Spectroscopic measurements, which PASTEL has, are more accurate than photomoetric measurements as done in Starhorse. We also compare the energy density contributions of the same set of stars between PASTEL and Starhorse to a random point in the ISM without considering extinction in Figure 4.1. Using the stellar parameters from PASTEL usually

yields a higher energy density value than when using the parameters from Starhorse.

We further analyzed the geometric attenuation in Figure 4.2 between the same set of stars as a sanity check to make sure that the methods being done to calculate stellar radii are relatively consistent with each other. It is important to consider not just the stellar radii, but the distance to the star as well as the catalogues do not usually agree on one value for the distance of stars. Additionally, through the algorithms to measure different stellar properties from these stars, there might be cases where some stellar parameters are being overestimated or underestimated. For this reason, if the geometric attenuation for the same set of stars is generally the same, we feel confident in continuing our calculations. We notice that these generally agree. Lastly, further tests like Figure 4.3, where the computed spectra for our set of stars is compared to literature values for the FUV energy density at Earth, give us confidence in continuing with this hierarchy.

4.2 Energy Density at the Sun

To make sure that the accuracy of the integrated u_{FUV} is not heavily underestimated due to not using the entire set of stars with our previously mentioned constraints, we calculated the total UV energy density at the location of the Sun. We found an integrated u_{FUV} of 6.57×10^{-14} [erg/cm^3], or slightly more that one Habing field [11]. Figure 4.3 shows the energy density spectra of our catalog. We compare our spectra with observations from [12] and [9]. [12] used an FUV spectrometer aboard the Apollo 17 spacecraft to observe the raw flux of about one-third of the sky which was later used to extrapolate to the total contribution coming from the entire sky. The details as to why this is a representative sample of the entire sky are not obvious, but this third is claimed to conform to the general set of dark and bright regions in the sky. The general trend of the spectra fits the observed values. Nonetheless, [9] values follow our spectra at these and longer wavelengths in our range. In Figure 4.3, the red[12] stars are slightly higher than the black[9] stars since the red stars were measured accounting for the total radiation field, while the black points

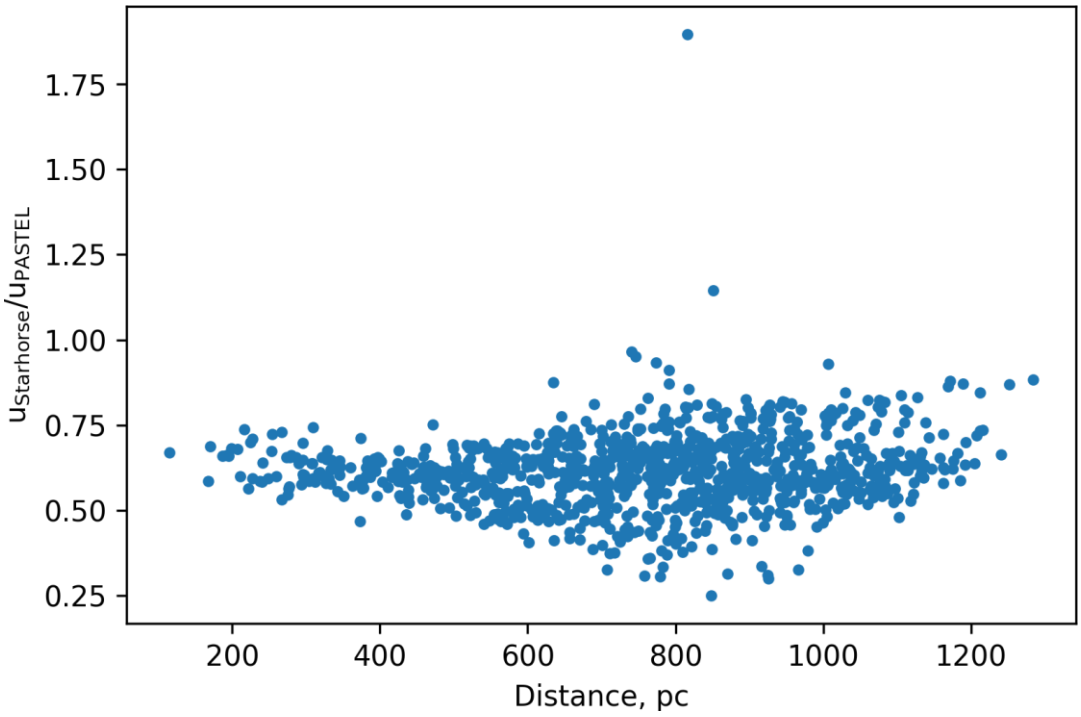

Figure 4.1: Energy density contribution comparison for the same set of stars between Starhorse and PASTEL at 1,000 random coordinates. The x-axis denotes the distance to the random points.

are only taking the direct radiation field into consideration, not the diffuse. The direct radiation field is simply light that traveled unaffected from one point to another. Hence, this does not include any scattered radiation sources. Additionally, the red points claim a $\pm$20% error, making our spectra be within these errors. The black points were measured by making a flux distribution of the sky in galactic latitude and longitude from a satellite with a spectrometer that made multiple measurements of 58012 stars distributed on the entire sky.

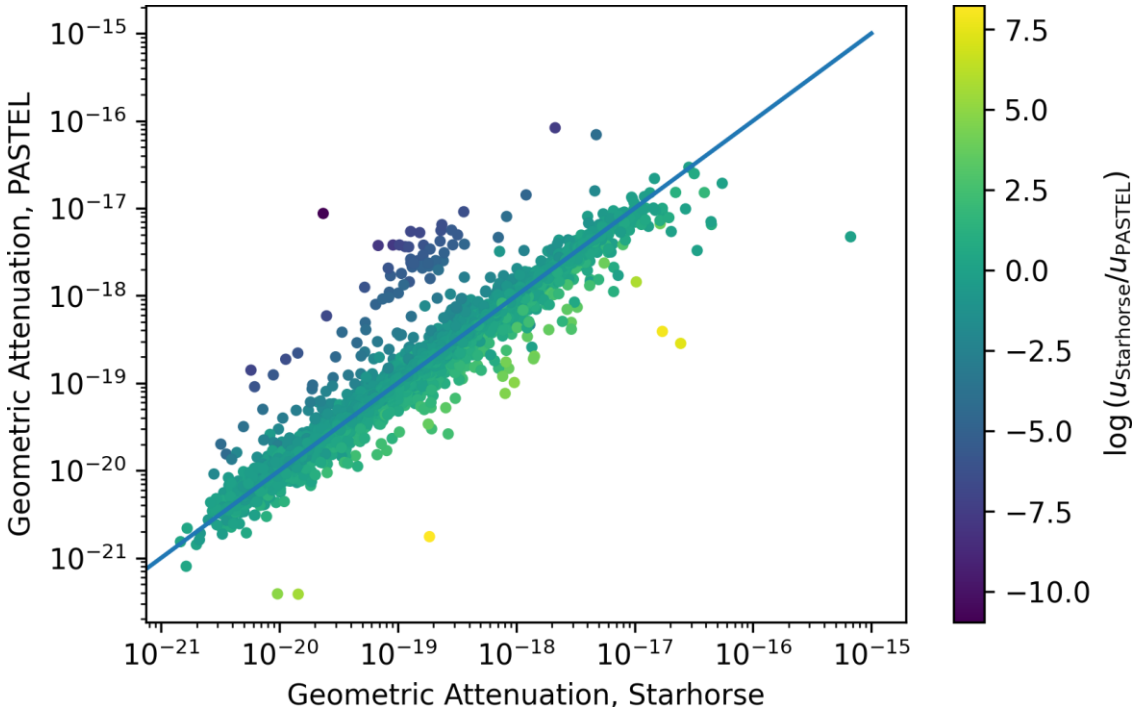

Figure 4.2: Geometric attenuation comparison for the same set of stars between Starhorse and PASTEL. Blue line denotes the 1:1 ratio line, and the color bar denotes the log base-10 ratio of the UV flux calculated from the Starhorse parameters to that calculated from the PASTEL parameters without considering the geometric attenuation or extinction.

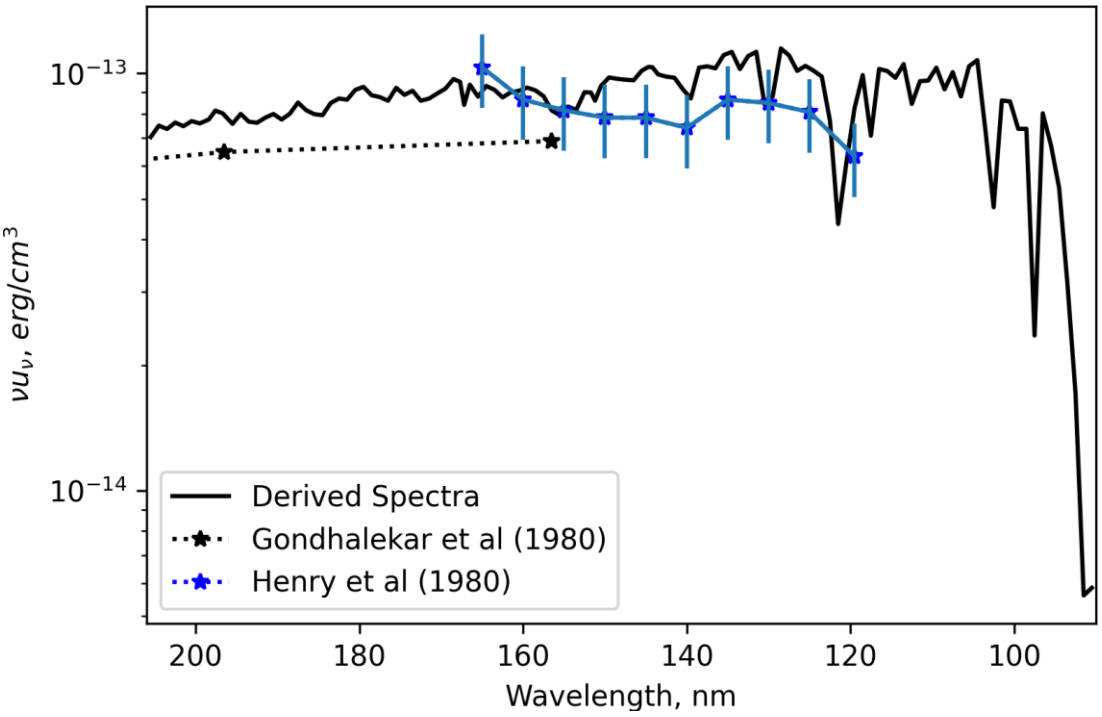

Figure 4.3: Derived spectra, considering extinction by [8], in the FUV range located at the Sun compared to observational values by [9] and [12] This calculated spectra made no further constraints on the catalogue sample mentioned in §3. Once integrated, the energy density is calculated to be 6.57×10^{-14} erg/cm^3. [9]'s diffuse measurements are not considered, only the direct ones as our model does not account for the diffuse radiation field.

There are also two highly regarded, yet distinct, values for the FUV field from Habing[11] and Draine [7]. Habing reports an energy density of 5.026×10^{-14} [erg/cm^3], or one Habing field, while Draine reports a value of 8.933×10^{-14} [erg/cm^3]. Habing used a generalized metric for the flux and extinction dependant for different wavelengths based on the star's spectral type using the set of stars from the *Bright Star Catalogue*. Draine referenced multiple literature and observational values at the time and derived an equation that is in

agreement with those results. This equation is as follows:

$$F(E) = 1.658 \times 10^6 (E/eV) - 2.152 \times 10^5 (E/eV)^2 + 6.919 \times 10^4 (E/eV)^3 \ , \qquad (4.1)$$

with the units being: photons/cm^2/s/sr/eV. The energy density value mentioned earlier comes from integrating this equation over energy Our results lie approximately halfway between these two measurements.

4.3 Map Size and Resolution

Figure 3.2 showed that around $\sim$90% of the energy density for stars up to 1.25 kpc is recovered for stars within $\sim$600 pc. Since we calculated an average value between one Habing field and one Draine field with the sample of stars going up to 1.25 kpc, we feel confident that we have a representative sample to determine the energy density in the ISM. Finding an appropriate size for the map while minimizing errors is not simple. For instance, if we consider a point 1.25 kpc away from us, the stars right outside of the dust map will become important to consider for the total FUV field.

In order to find an appropriate size for the map, we made a sample calculation at two different coordinates of the FUV energy density without extinction coming from stars within the dust map and outside of the dust map. The sample of stars from outside of the dust map also come from PASTEL and Starhorse. We calculated the percentage of the contribution to the FUV field of the stars within the dust map and outside of the map at a distance of 800 pc in $\hat{x}$ and $\hat{z}$. The importance of labeling these is that stellar populations are more prominent the closer to the galactic center, and the stellar population density and extinction decreases the more we move from the galactic plane. At (800, 0, 0) pc, we found that the stars within the dust map contribute 83% of the total FUV field at that point. It is to be mentioned that this result would be better had extinction been considered. Dust density generally increases as one approaches the galactic center. Therefore, light from the stars outside of the dust map would have been attenuated by a larger factor than the

stars within the dust map, without considering that the geometric attenuation would also be a factor as well. Ultimately, the combination of these two, the greater distances, and therefore a likely higher dust extinction would have yielded better results. Figure 4.4 shows the average fraction of the total energy density coming from stars within the dust map for varying distances from the Sun. The fraction is held generally constant, with a spike at $\sim$100 pc. This spike is caused by a hot star too that was too close to one of the points of calculation. Even though the fraction is held generally constant at a distance similar to the dust map, we chose a smaller size of 800 pc to have a safety margin on errors that we may not be accounting from stars right outside of the dust map.

At (0, 0, 800) pc, the stars outside of the dust map do contribute a more considerable amount however. The stars within the dust map contributed 58% of the total FUV field at that point. Since the calculation is carried out without considering extinction, the geometric attenuation, or solely the distance, must have been the factor that made these calculations relatively the same. In other words, distances to stars outside of the dust map does increase, but does not increase a significant amount to attenuate the total contribution from these stars relative to the stars within the dust map, which are considerably closer.

We therefore make a map of radius 800 pc so as to not compromise the energy density values towards the edge of the map, although varying in $z\hat{}$ must be done with caution.

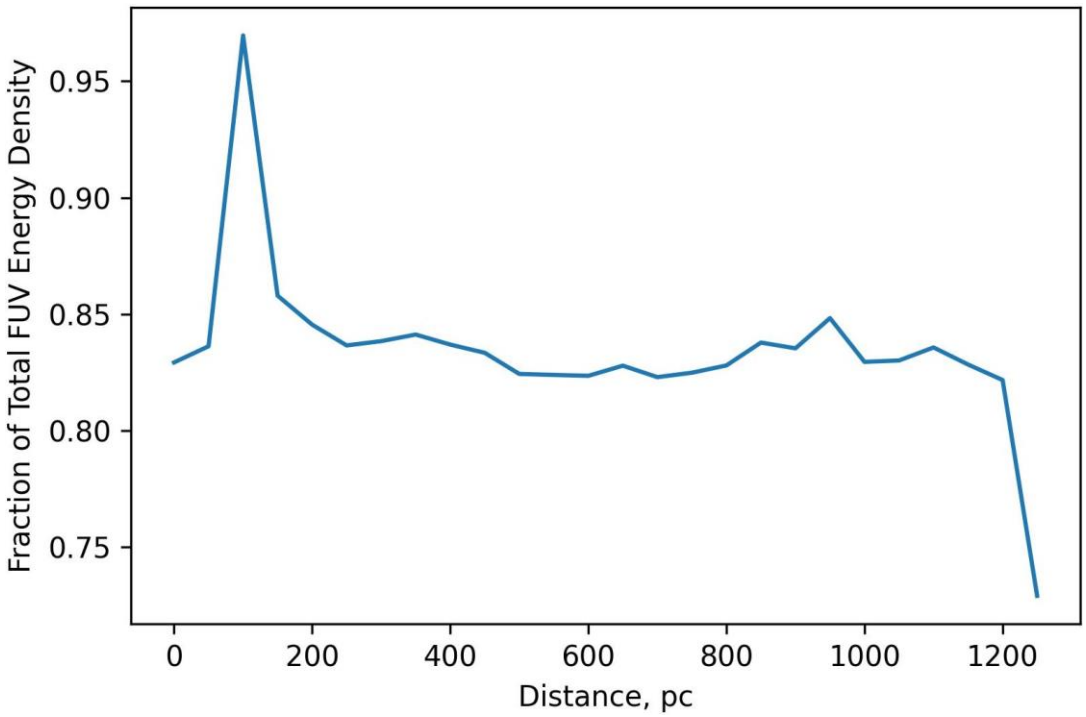

Figure 4.4: Fraction of the total energy density of the stars within the dust map compared to stars from within and outside of the dust map as a measure of distance from the Sun on the z = 0 plane without extinction. For a point (d, u), u is the average fraction of the energy density around a circle of radius d with jumps of 15°.

Chapter 5

Results and Discussion

5.1 FUV Field vs. Dust Map

Visually speaking, there is a correlation between the resultant FUV field and the dust density denoted by the dust map as shown in Figure 5.1. Regions with higher energy density in our map almost directly correlate to regions of low dust density, and the inverse is also true. We also notice smaller brighter regions, or grids, which belong to high temperature stars. The spread, or continuity, of these regions tell if whether this higher energy density is due to high temperature stars or stars that happened to be close to the center of the grid. To properly analyze the relation between the dust density and the energy density, we plot the median energy density value for a logarithmically spaced dust density range, as well as the dust density for each star in the catalogue and compared it with their temperatures.

For the first case, in Figure 5.3, we can notice that there is a general rising trend for the median energy density as a measure of the dust density with a sharp peak at the higher dust density. This peak is caused by low number statistics as there are 3 cells with said gas density range.

When we compare the dust density of each star in their respective voxel within the dust map, we find that there is a relation between the gas density surrounding a star and its temperature.

We also consider the probability density of finding a star with a given temperature T, to have a surrounding dust density n in Figure 5.5. This should provide some insight into the general spread of dust around stars of certain temperatures. This, alongside Figure 5.3, tell us that there is little to no relation between the energy density or the temperature of

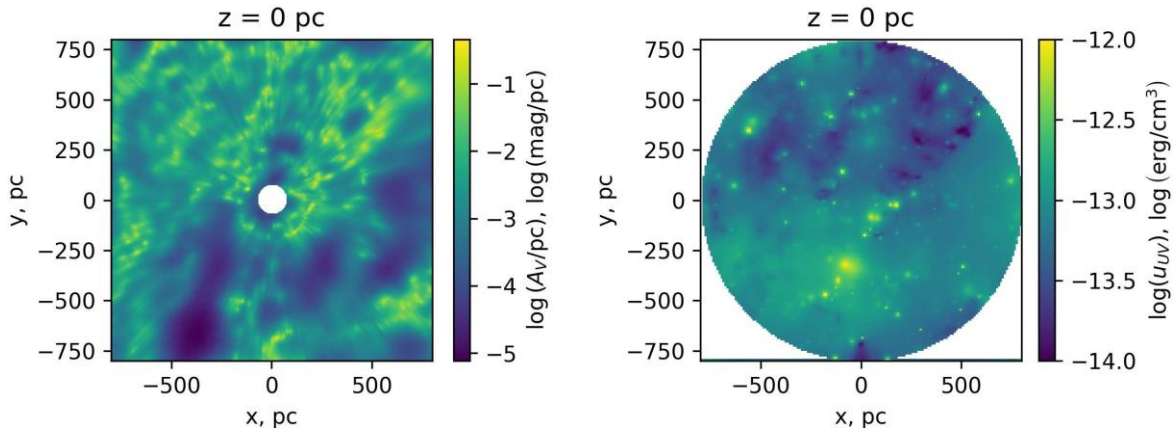

Figure 5.1: Slice of the dust map (left) and the FUV map (right) at z = 0. The anti-correlation between the dust density denoted by the brighter colors in the left plot and the energy density denoted by the dimmer colors in the plot to the right is apparent. The opposite, the lack of dust and the higher energy density, is also apparent. The 69 pc hole of the dust density is also shown in the left plot.

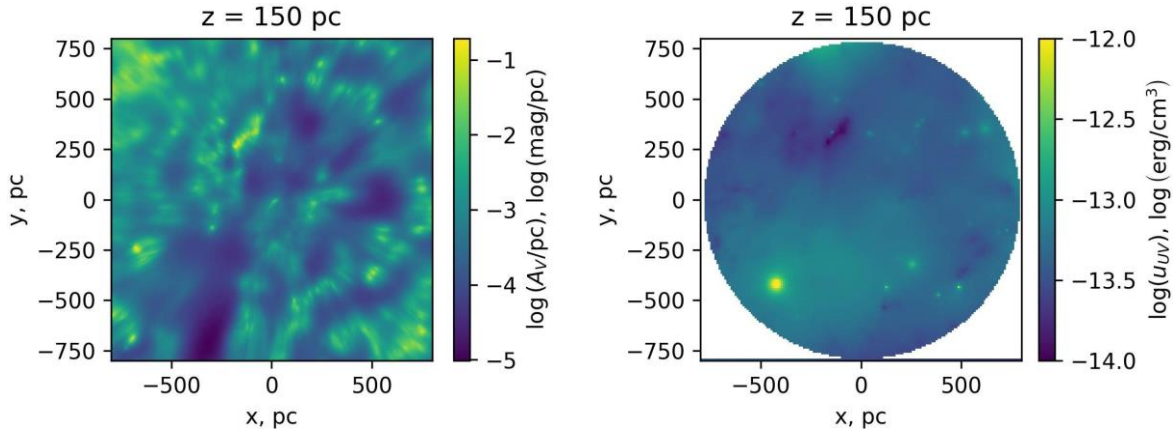

Figure 5.2: Slice of the dust map (left) and the FUV map (right) at z = 150 pc. The same anticorrelation as Figure 5.1 is shown. In the energy density plot, to the bottom left, star BD-03 2178 is shown, with a T_{eff} of 44,500K and R = 13.26 $R_\odot$. This plot also demonstrates that the density of stars decreases as one moves away from the galactic plane.

stars and the dust density. Extreme cases like the ones with high energy density and high temperature stars are not clearly detailed however.

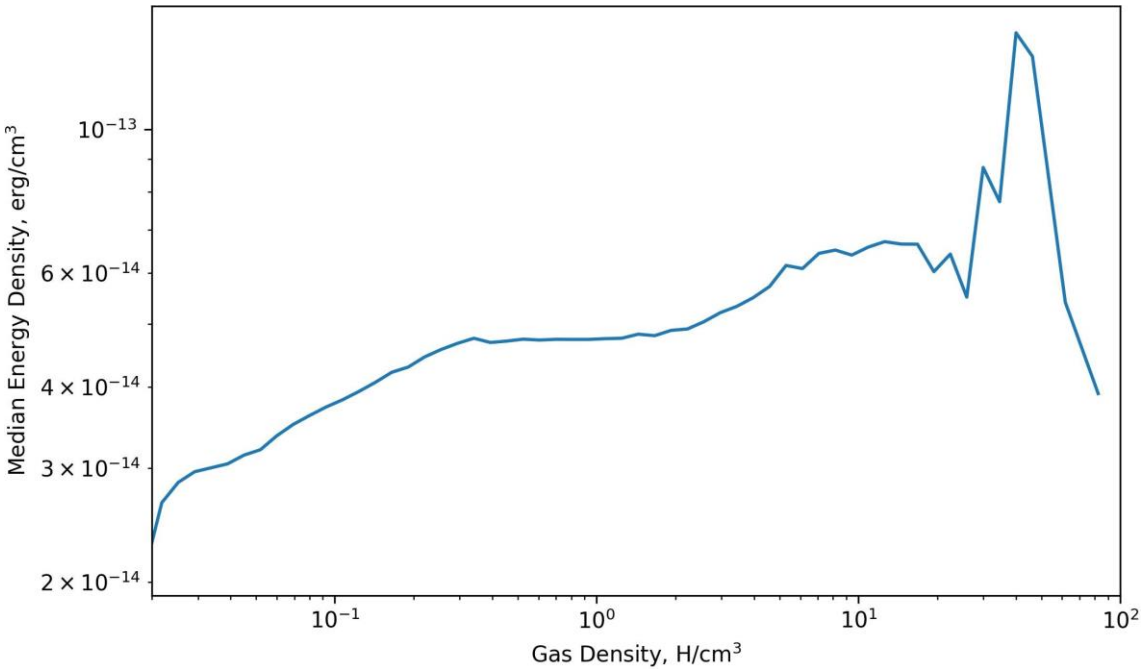

Figure 5.3: Median FUV energy density as a measure of the gas density correlating the dust map and the energy density map covering the entire set of *z* values. Since the dust map consists of 5*5*5 pc^3 grids, and the energy density map consists of 10*10*10 pc^3 grids, the average of the 8 dust density grids within each energy density grid is taken.

Gas density is equated as:

$$\frac{1A_V}{pc} = \frac{2\times10^{21}[\mathrm{H/cm^2}]}{1\mathrm{pc}} \Big/ \frac{1\mathrm{pc}}{3.086\times10^{18}\mathrm{cm}} = 6.48 \times 10^{2} \ \frac{\mathrm{H}}{\mathrm{cm^3}}$$

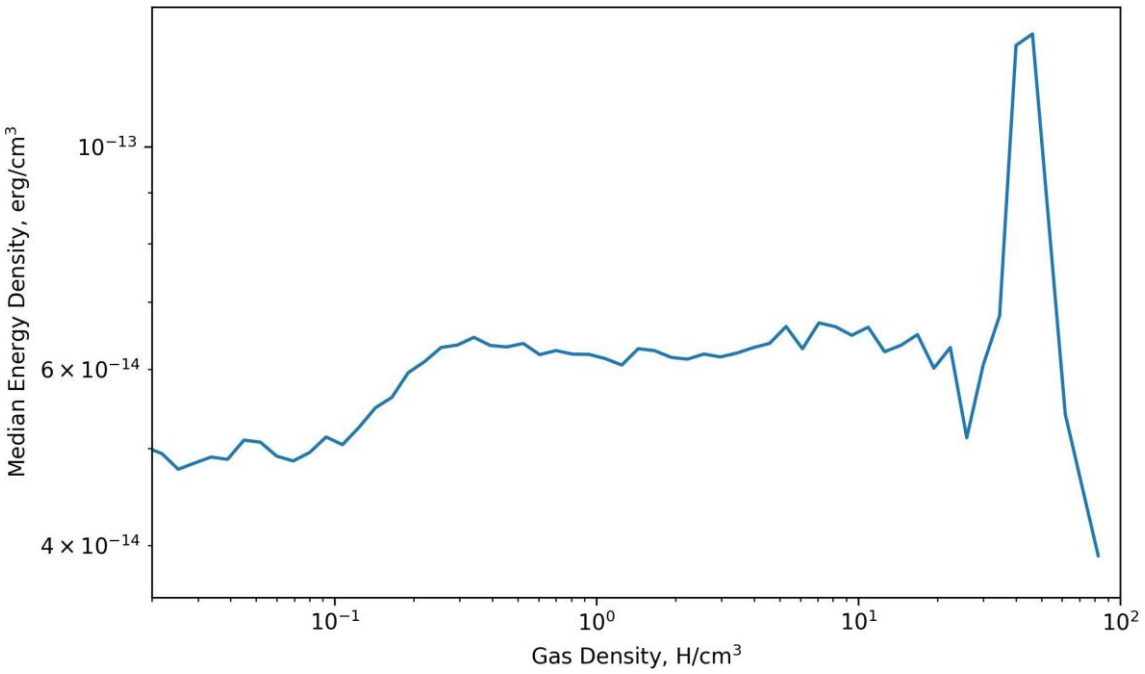

Figure 5.4: Same as Figure 5.3, but constrained to $|z| \leq 50$pc. We find a more even, but still rising, distribution for the dust density. Just as Figure 5.3, the values at high dust density are spiked due low number statistics. There is only one grid within the spikes ($N_H > 10^{-13}$H/cm^3).

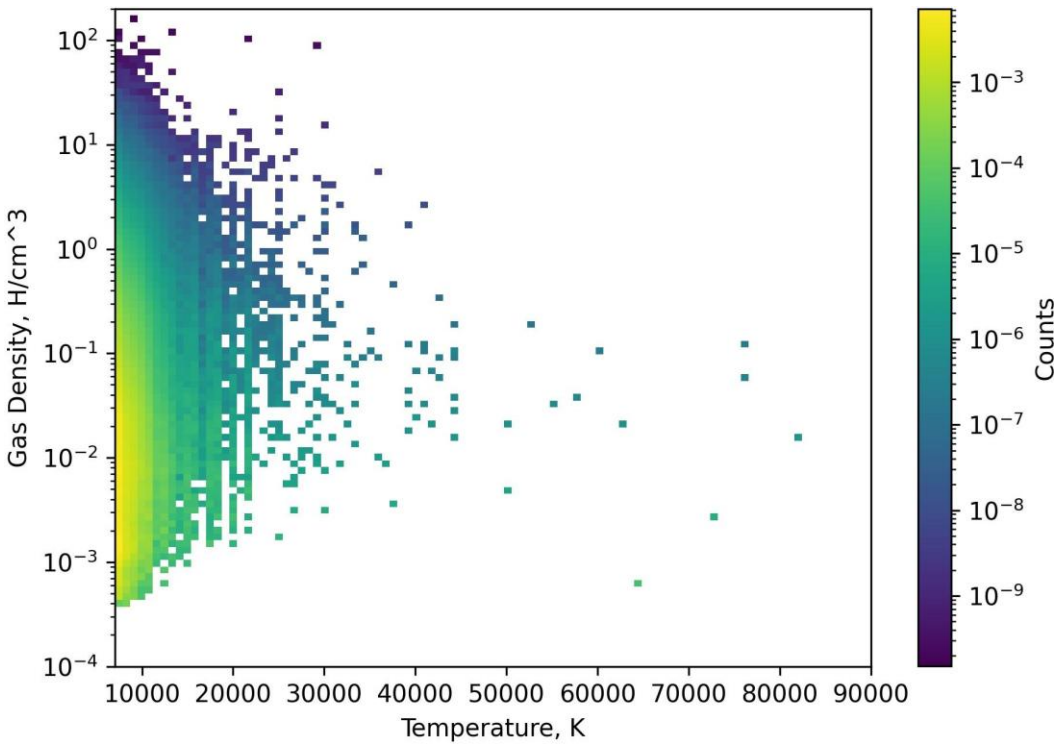

Figure 5.5: Gas density measurement at the voxel of each star in the set of stars used to calculate the energy density map with their temperature. The color demonstrates the probability density P (n, T) of finding a star within some logarithmically spaced n and temperature T where the probability density is calculated as:

P = (counts/(sum of counts $*$ area of bin)).

.

Chapter 6

Conclusion

I present an 800 pc radius map of the FUV energy density in the local ISM. By using a set of 857,209 stars coming from PASTEL and Starhorse, a 1.25 kpc dust map, and stellar models for varying surface gravities and temperatures, I calculated the FUV energy density of the local ISM for voxels of size 10*10*10 pc^3. While the map extends to great distances, it is advisable to remain within 800 pc of the Sun as errors are more prominent the further out one goes. I also found that there is a direct relation between the dust and energy densities, as it was initially expected by the qualitative anticorrelation between the dust and FUV energy density maps.

This map has the intent of aiding the future study of the ISM in general, but mainly aids in the study of molecular clouds. Grids with high $\hat{z}$ must be used with caution as the UV field here may be missing a substantial amount of flux, which originates from far-away stars that we do not consider.

References

[1] F. Anders, A. Khalatyan, A. B. A. Queiroz, C. Chiappini, J. Ardèvol, L. Casamiquela, F. Figueras, Ó. Jiménez-Arranz, C. Jordi, M. Monguió, M. Romero-Gómez, D. Altamirano, T. Antoja, R. Assaad, T. Cantat-Gaudin, A. Castro-Ginard, H. Enke, L. Girardi, G. Guiglion, S. Khan, X. Luri, A. Miglio, I. Minchev, P. Ramos, B. X. Santiago, and M. Steinmetz. Photo-astrometric distances, extinctions, and astrophysical parameters for Gaia EDR3 stars brighter than G = 18.5. , 658:A91, February 2022.

[2] Michael Bessell and Simon Murphy. Spectrophotometric Libraries, Revised Photonic Passbands, and Zero Points for UBVRI, Hipparcos, and Tycho Photometry. , 124(912):140, February 2012.

[3] D. Scott Birney, Guillermo Gonzalez, and David Oesper. *Observational Astronomy*. Cambridge University Press, 2 edition, 2006.

[4] Jason A. Cardelli, Geoffrey C. Clayton, and John S. Mathis. The Relationship between Infrared, Optical, and Ultraviolet Extinction. , 345:245, October 1989.

[5] F. Castelli and R. L. Kurucz. New Grids of ATLAS9 Model Atmospheres. In N. Piskunov, W. W. Weiss, and D. F. Gray, editors, *Modelling of Stellar Atmospheres*, volume 210, page A20, January 2003.

[6] F. Castelli and R. L. Kurucz. New Grids of ATLAS9 Model Atmospheres. In N. Piskunov, W. W. Weiss, and D. F. Gray, editors, *Modelling of Stellar Atmospheres*, volume 210, page A20, January 2003.

[7] B. T. Draine. Photoelectric heating of interstellar gas. , 36:595–619, April 1978.

[8] Gordian Edenhofer, Catherine Zucker, Philipp Frank, Andrew K. Saydjari, Joshua S. Speagle, Douglas Finkbeiner, and Torsten Enßlin. A Parsec-Scale Galactic 3D Dust

Map out to 1.25 kpc from the Sun. *arXiv e-prints*, page arXiv:2308.01295, August 2023.

[9] P. M. Gondhalekar, A. P. Phillips, and R. Wilson. Observations of the interstellar ultraviolet radiation field from the S2/68 sky-survey telescope. , 85(3):272–280, May 1980.

[10] Munan Gong, Eve C. Ostriker, and Mark G. Wolfire. A Simple and Accurate Network for Hydrogen and Carbon Chemistry in the Interstellar Medium. , 843(1):38, July 2017.

[11] H. J. Habing. The interstellar radiation density between 912 A and 2400 A. , 19:421, January 1968.

[12] R. C. Henry, R. C. Anderson, and W. G. Fastie. Far-ultraviolet studies. VII - The spectrum and latitude dependence of the local interstellar radiation field. , 239:859–866, August 1980.

[13] Alex S. Hill, Mordecai-Mark Mac Low, Andrea Gatto, and Juan C. Ibáñez-Mejía. Effect of the Heating Rate on the Stability of the Three-phase Interstellar Medium. , 862(1):55, July 2018.

[14] B.S. Ryden and B.M. Peterson. *Foundations of Astrophysics*. Addison-Wesley, 2010.

[15] Caroline Soubiran, Jean-François Le Campion, Nathalie Brouillet, and Laurent Chemin. The PASTEL catalogue: 2016 version. , 591:A118, June 2016.

[16] M. G. Wolfire, D. Hollenbach, C. F. McKee, A. G. G. M. Tielens, and E. L. O. Bakes. The Neutral Atomic Phases of the Interstellar Medium. , 443:152, April 1995.

[17] Mark G. Wolfire, Christopher F. McKee, David Hollenbach, and A. G. G. M. Tielens. Neutral Atomic Phases of the Interstellar Medium in the Galaxy. , 587(1):278–311, April 2003.

[18] Xiangyu Zhang, Gregory M. Green, and Hans-Walter Rix. Parameters of 220 million stars from Gaia BP/RP spectra. , 524(2):1855–1884, September 2023.

Curriculum Vitae

David Alejandro Lomeli graduated from Douglas High School, Douglas, AZ, in the spring of 2018. He entered the University of Arizona in the upcoming fall where he graduated with a Physics and an Astronomy major and a minor in Mathematics in the spring of 2022. While pursuing his bachelor's degree, he did an internship at NASA for a semester and also worked as a mathematics tutor during his last two semesters at C.A.T.S. Academics.

To continue his studies, in the fall of 2022, he entered the University of Texas at El Paso to pursue a master's degree in Physics. Throughout his time at UTEP, he has worked as a Teaching and Research Assistant, and gave a talk at the 39^{th} Annual New Mexico Symposium. He is now expected to graduate with said degree in the spring of 2024.

Email address: davidalomeli@hotmail.com